Journal of Materials Chemistry A

Accepted Manuscript

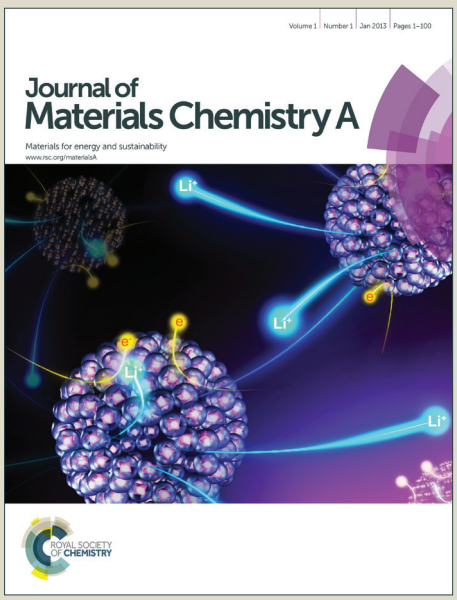

ROYAL SOCIETY OF CHEMISTRY

www.rsc.org/materialsA

A Simple and Scalable Approach to Hollow Silicon Nanotube (h-SiNT) Anode Architectures of Superior Electrochemical Stability and Reversible Capacity

Rigved Epur[a], *Prashanth Jampani Hanumantha*[b], *Moni K. Datta*[b], *Daeho Hong*[b], *Bharat Gattu*[c] *and Prashant N. Kumta*[a,b,c,d,e],*

[a]Department of Mechanical Engineering and Materials Science (MEMS), University of Pittsburgh, 3700 O' Hara Street, Pittsburgh, Pennsylvania, USA

[b]Department of Bio Engineering, University of Pittsburgh, 3700 O' Hara Street, Pittsburgh, Pennsylvania, USA

[c]Department of Chemical and Petroleum Engineering, University of Pittsburgh, 3700 O' Hara Street, Pittsburgh, Pennsylvania, USA

[d]Center for Complex Engineered Multifunctional Materials (CCEMM), University of Pittsburgh, 3700 O' Hara Street, Pittsburgh, Pennsylvania, USA

[*]Corresponding author. E-mail: pkumta@pitt.edu

815C Benedum Hall

3700 O'Hara Street

Pittsburgh, PA 15261

Tel: (412) 648-0223

Keywords: lithium-ion batteries; silicon nanotubes; anodes; sacrificial template; magnesium oxide

ABSTRACT

Strain engineered unique architectures of silicon nanotubes have garnered tremendous attention as high capacity and stable lithium-ion battery (LIB) anodes. However, the expensive nature of the hitherto synthesis techniques used to produce the silicon nanotubes combined with the inferior yield and poor loading densities have rendered these unique morphologies unattractive for commercial LIB systems. In this study, we report for the first time, a simple, facile, and more importantly, recyclable sacrificial template based approach involving magnesium oxide (*MgO*) nanorods for producing scalable quantities of hollow silicon nanotubes (h-SiNTs) architectures. Electrodes fabricated from these h-SiNTs derived from this novel scalable approach exhibit equitable loadings and reversible capacities in excess of 1000 $mAh.g^{-1}$ at a high current density of $2A.g^{-1}$ for nearly 400 cycles, combined with a very low fade rate of only 0.067 % loss per cycle. The high capacity, good current rate characteristics combined with excellent charge-transfer kinetics as well as the long cycle life of these engineered h-SiNTs render this approach viable for industry scale while also boding promise for practical applications.

1. Introduction

Lithium ion (Li-ion) batteries (LIBs) among the existing battery technologies have attracted immense attention due to their flexible design, high energy and power densities. Hence LIBs have emerged as the prime choice of preferred energy storage devices for a plethora of applications such as portable and consumer electronics as well as electric vehicles.[1] The current state-of-the art battery chemistry used in commercial Li-ion battery devices comprise a graphite based anode along with a cathode belonging to either layered materials ($LiCoO_2$, $LiNiO_2$, etc.,), spinels ($LiMn_2O_4$) or olivine based structures ($LiFePO_4$), which exhibit energy

densities in the range of 100-260 $Wh.kg^{-1}$. However, the ever growing demand for a longer lasting high energy density battery in portable electronic devices equipped with myriad energy intensive multi-faceted applets combined with a larger driving range for electric vehicles has created an even greater impetus to develop the still elusive higher performing Li-ion batteries displaying even higher energy densities and longer cycle life than those afforded at present. The target of meeting such stringent demands clearly necessitates the identification and development of novel cathodes and anode materials.

Accordingly, the pursuit of high energy density anode materials has led to the identification of silicon which has over the recent years emerged as an obvious choice as an alternative anode to graphite. This is primarily owing to its ability to alloy with Li at low electrode potentials and store nearly 10 fold more charge than graphite due to the formation of maximum lithium containing alloy phase, $Li_{22}Si_5$ having a theoretical capacity of 4200 $mAh.g^{-1}$. Although attractive with the high specific capacity, bulk commercial silicon undergoes colossal volume changes (>300%) during the lithiation and de-lithiation processes, resulting in an overwhelming volume expansion related stresses that lead to the fracture of the active material. The ensuing electrochemical reaction related fracture, typically known as pulverization results in active material isolation that leads to the loss of electrical contact with the current collector, a 'decrepitation' phenomenon that eventually results in complete loss in capacity or rapid capacity fade. Furthermore, fracture of the active material results in the formation of new surfaces, which act as additional sites for the solid electrolyte interphase (SEI) formation, wherein, additional *Li* is consumed during this process, contributing to further deterioration and loss in capacity with concomitant reduction in coulombic efficiency.

There have been myriad approaches outlined in the literature with varying degrees of seemingly putative perfection to address the above mentioned challenges encountered in bulk silicon anodes. These approaches include reduction in particle size, use of *in-situ* and *ex-situ*

generated active-inactive composites and strain engineered nanostructures that have been identified to suppress the capacity fade by alleviating the stresses generated during electrochemical cycling. Among the several nanostructures of silicon identified i.e., nanowires,[2, 3] core-shell heterostructures,[4-8] nanoshells,[8, 9] etc. hollow silicon nanotubes[10-13] have attracted tremendous interest due to their high capacity and excellent cyclability with minimal capacity fade, arising from its unique nanostructure enabled mechanical properties. Silicon nanotubes offer facile strain similar to the one dimensional silicon nanowires and furthermore, the free volume available due to the hollow tubular configuration combined with the hoops stress allows the silicon to freely expand/contract without undergoing fracture. Moreover, the nanotube configuration exhibits good rate characteristics by offering shorter Li^+ diffusion distances and increased wetting of the electrolyte on the inner and outer surfaces of the nanotube.[12] Initial studies published on silicon nanotubes have reported capacities >3000 $mAh.g^{-1}$ with more than 85% capacity retention.[11, 12] More recently, an SEI controlled double walled silicon nanotubes has also been reported to exhibit excellent capacity retention for 6000 cycles.[10]

Apart from these reports describing approaches to augment the materials characteristics and electrochemical properties, other factors that play an equally important role when selecting battery materials from a commercialization standpoint are: cost of the raw materials or precursors used for fabrication, the synthesis technique, recyclability of the precursors and the various fabrication steps as well as recycling costs, and ensuing environmental effects of the by-products generated from the production processes. Despite their excellent electrochemical characteristics, the silicon nanotubes mentioned above, and reported in the literature are typically prepared by synthesis techniques that require large volumes of expensive inorganic solvents, expensive sacrificial templates. Furthermore, these approaches suffer from lower product yield and inferior loading densities. For example, the

first report on using silicon nanotube anode as the Li-ion anode required the use of expensive porous alumina membrane templates and glyme based organic solvents.[12] In another follow up study, arrays of sealed hollow silicon nanotubes were grown directly on metallic substrates using sacrificial *ZnO* nanorod templates which exhibited good capacity and cyclability.[11] However, such substrate growth process is unfavorable from an industrial standpoint where slurry casting methods are typically employed to achieve desired loading densities. The double walled hollow silicon nanotube anodes developed by Wu *et al*, use a relatively inexpensive technique but the low loadings (0.02 to 0.1 $mg.cm^{-2}$) achieved by this method however render them unattractive for practical applications wherein higher loadings or areal capacities are required to match the corresponding equivalent cathode loadings and capacities.[10] More recently, Lu *et al*[13] synthesized carbon decorated silicon nanotubes using a benign approach wherein the silicon nanotubes are made by depositing silicon via a vapor phase transport onto *ZnO* nanorod arrays by heating a mixture of *SiO/Si*. Though impressive capacities (>2000 $mAh.g^{-1}$) with good capacity retention are achieved by this method, this approach requires very long processing times (6-12 hours for preparing *ZnO* templates and another 16 hours for silicon deposition) and the overall yield from such processes is often low.

Therefore, in order to render these silicon nanotubes as an industrially viable and economically and environmentally benign anode system that can potentially replace graphite, it is very critical to adopt a synthesis route that utilizes inexpensive precursors, involves the engagement of unsophisticated equipment and more importantly, is capable of producing large yield of nanotubes that could eventually be amenable for slurry casting processes utilized in contemporary battery processing techniques. Following a careful and prudent analysis of the existing methods reported for generating silicon nanotubes, we hypothesize that the production of the sacrificial template appears to be the primary major bottle-neck in achieving the aforementioned attributes desired for achieving an efficient electrode design. In

this study therefore, we propose a synthesis approach wherein, large quantities of *MgO* nanorods were synthesized using a hydrothermal technique utilizing inexpensive precursors. These nanorods serve as the sacrificial template onto which silicon is deposited as a thin layer by chemical vapor deposition. The core-shell structure thus formed is treated with an acid to dissolve the inner core (*MgO* nanorods) without affecting the Si thereby obtaining the desired hollow silicon nanotubes. **Figure 1** shows the schematic representing the steps involved in the formation of the h-SiNTs from the *MgO* nanorods prepared by the hydrothermal process. Furthermore, a completely successful and efficient regenerative process was developed using simple, high yield precipitation techniques to recover the original precursors which could then be reused to synthesize subsequent batches of *MgO* nanorod templates that can then be further used to generate the electrochemically active hollow Si nanotubes (h-SiNTs).

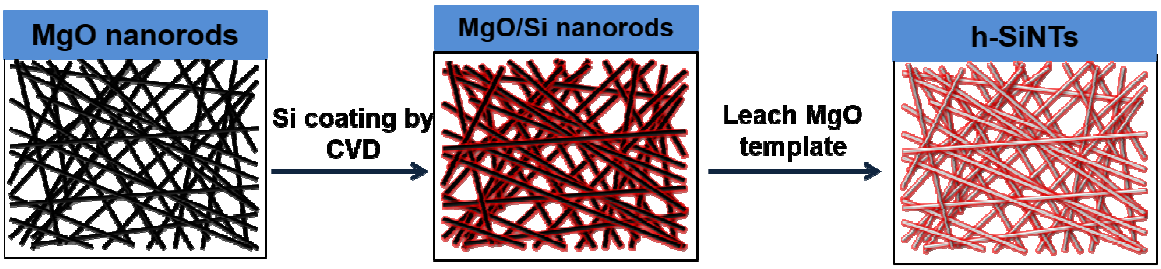

Figure 1: Schematic showing the morphological evolution of hollow silicon nanotubes (h-SiNTs) from the hydrothermally synthesized magnesium oxide (MgO) nanorods.

2. Results and Discussion

Synthesis of Silicon Nanotube

Hydrothermal synthesis approach is a simple and commercially viable method as it is capable of generating large amounts of the product in a short period of time and uses inexpensive and simplified equipment. The effect of high pressure conditions, which is usually generated inside the autoclave reactor lead to improved kinetics allowing for faster diffusion of chemical species. This mechanism enables the chemical reactions to occur at relatively lower temperatures in the hydrothermal reactor compared to hitherto approaches via a solid state reaction or heating in an open reactor system. In this work accordingly, hydrated magnesium acetate *($Mg(CH_3COO)_2.4H_2O$)* was used as the precursor for *MgO* generation and urea served as the combustion agent for the suitable and appropriate decomposition of magnesium acetate according to **Reaction 1**.

$$Mg(CH_3COO)_2.4H_2O + CO(NH_2)_2 + \tfrac{3}{2}O_2 \rightarrow Mg(OH)_2 + 2CH_3COOH + CO_2 + N_2 + 4H_2O$$

(Reaction-1)

The final product collected over the PTFE membrane at the end of the washing step was a white, fibrous thick cake that was subsequently calcined in the presence of oxygen gas for several hours to convert the magnesium hydroxide to magnesium oxide (*MgO*) according to **Reaction 2**. A multi-stage and slow heating rate is important in order to preserve the morphology of the *MgO* nanorods. Heating rapidly could cause fracture of the rods due to rapid evaporation of moisture and other volatile species present inside the pores of the nanorods.

$$Mg(OH)_2 \rightarrow MgO + H_2O$$

(Reaction 2)

The yield of the *MgO* cake obtained at the end of the calcination step was found to be approximately 1g, which corresponds to an approximate conversion rate of 85% from magnesium acetate to magnesium oxide. The *MgO* cake obtained after the calcination step is shown in **Figure 2a**. Even after the calcination step, the cake structure was still maintained presenting sufficient strength and integrity allowing the cake to be lifted using tweezers and amenable for transportation into the CVD reactor for subsequent silicon deposition. This is indeed very advantageous from a practical standpoint; as it is easier to employ the template in the form of a solid cake instead of loose powders for easy handling, insertion and removal from the CVD reactor. The silicon deposition was furthermore, performed using a method similar to previously reported and published approaches from our group for generating CNT/Si heterostructures.[5, 6, 14] The deposition was carried out at 500°C in a low pressure CVD reactor using 2% silane (diluted in ultra-high purity (UHP) argon gas). The *MgO* cake was placed at the center of the reactor on a quartz slide. Silicon deposition was then carried out for 10 minutes to form a uniform thin layer of silicon coating on the surface of the *MgO* nanowires. After the deposition was complete, the reactor tube was allowed to cool to room temperature under the flow of argon gas before it was opened to avoid any oxidation of the nanotubes during retrieval.

The obtained *Si/MgO* core-shell structure was then treated with hydrochloric acid (*HCl*) to dissolve the core or the oxide nanorod template to yield the hollow nanotubes of silicon. The dissolution of *MgO* template in *HCl* occurs according to the following reaction (**Reaction 3)**:

$$MgO + 2HCl \rightarrow MgCl_2 + H_2O$$

(Reaction 3)

After a series of washing steps using DI water and isopropyl alcohol (IPA) to remove the dissolved $MgCl_2$ or any other unwanted impurities, the final product containing the hollow silicon nanotubes (h-SiNTs) are collected on top of the PTFE membranes. After drying, the h-SiNTs can be collected in the form of a cake (shown in **Figure 2b**) which can be easily dispersed in aqueous or non-aqueous solvents using ultra sonication for generating the slurries for electrode fabrication. In this case, nearly 0.5 g of h-SiNTs (using ~1g of *MgO* nanorods) is obtained from the execution of a short 15 minute CVD deposition of silicon in the reactor. The yield of the *MgO* nanorods can easily be scaled up to several kilograms by employing larger autoclave vessels, capable of holding several hundred gallons of the initial precursors which are easily commercially available. Also, a similar scale up method for silicon deposition can be envisioned by using large Si-CVD reactors that are typically used in the photovoltaic and semiconductor industry and can accommodate bulk quantities of *MgO* nanorod cakes (weighing several kilograms) as templates for subsequent amorphous (*a-Si*) deposition. Thus, it can be envisioned that upon elimination of the template by dissolution in acid followed by washing with water, several kilograms of h-SiNTs can be obtained from a single batch of the sacrificial nanorod template demonstrating the efficacy of the approach.

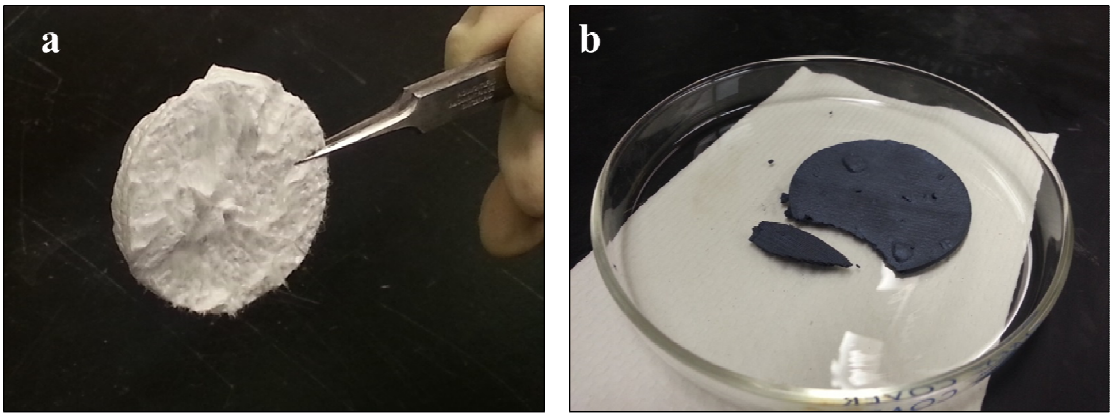

Figure 2: (a) MgO nanorod cake obtained after calcining $Mg(OH)_2$ and (b) Hollow silicon nanotube (h-SiNT) cake obtained after leaching the MgO nanorod template using HCl.

Materials Characterization

Phase analysis and crystal structure of the composites comprising the sacrificial *MgO* nanorod template; core-shell structure containing the *MgO* nanorods and silicon coating; and the resultant hollow silicon nanotubes (h-SiNTs) obtained after template dissolution was performed and determined using x-ray diffraction analysis. **Figure 3a**, shows the x-ray diffraction patterns of the nanocomposites generated during the various stages of the synthesis process. It can be observed that the x-ray pattern for the sacrificial template is only composed of peaks corresponding to *MgO*, indicating the complete conversion of the magnesium acetate precursor to the corresponding oxide during the hydrothermal and calcination processes. After the silicon deposition, two broad peaks at 2θ angles of 28° and 55° are observed in the diffraction pattern, indicative of the presence of an amorphous phase. The location of these broad peaks correspond to the first and second short range radial distribution order for amorphous silicon and is consistent with our previous reports related to amorphous silicon obtained on multiwall carbon nanotubes (MWCNTs) grown using similar conditions.[4]

After the acid etching process, the x-ray diffraction pattern do not contain any crystalline peaks that correspond to any remnant phase of the template, *MgO* or that of $MgCl_2$

precursor which is formed during the etching process, thereby indicating the complete dissolution and a thorough successful step involving washing and removal of the sacrificial template. The presence of amorphous silicon was further confirmed by collecting the Raman spectra obtained on the final cake obtained after the acid etching process. Previous studies indicate that the presence of a sharp peak at 520 cm^{-1} in the Raman spectra corresponds to the transverse optical (TO) phonon mode characteristic of crystalline silicon.[15-17] As the crystallite size or the long range order decreases for silicon, the peak expectedly becomes broader and shifts to lower wavenumbers. The Raman spectra (see **Figure 3b**) of the final obtained cake show the presence of a broad peak at 480 cm^{-1} which corresponds to that of amorphous silicon and is consistent with the previous reports obtained.[4, 18-20] The presence of Si was also validated by EDAX analysis discussed in the supporting section (see **Figure S1**).

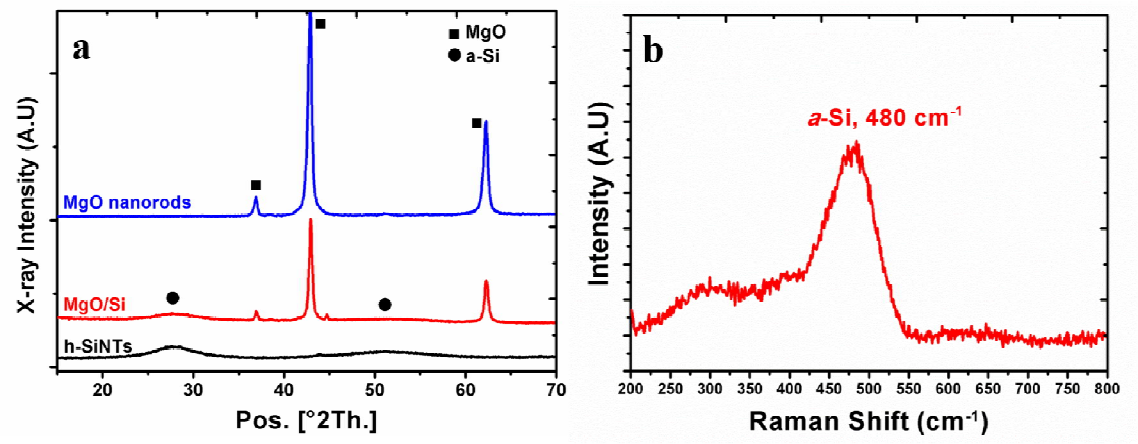

Figure 3: (a) XRD patterns of calcined MgO, core-shell MgO/Si and h-SiNTs formed after leaching MgO nanorods and (b) Raman spectra obtained on the h-SiNTs after leaching MgO nanorods.

The morphology of the nanostructures (*MgO* nanorods, silicon coated MgO nanorods and h-SiNTs) formed at different stages of the process were analyzed by scanning electron

microscopy (SEM) and are shown in **Figure 4.** These images indicate that the final product contains only one dimensional (1-D) structures or presence of nanorods. The nanorods appear to have varying lengths ranging from few microns to a maximum of 200 μm. The diameters varied from 0.5 μm to 1 μm. This large variation in the dimensions of the nanorods can be attributed to the extremely dynamic and harsh conditions prevalent in the autoclave during the hydrothermal reaction processes, resulting in the rapid nucleation and growth of the nanorods that could also simultaneously lead to fracture of the nanorods causing the large variation in geometry and length. The morphology of the nanorods template however, is extremely important since the silicon deposited in the subsequent step would also acquire and assume this template morphology to yield the hollow nanotubes since the formation of silicon follows nucleation and growth following a pseudo-morphous mechanism similar to all template based approaches. Despite the large variation in the dimensions of the *MgO* nanorods template, no other morphologies such as particles or aggregates are observed. Additionally, as seen from the **Figure 4(a)**, it can be observed that the surface of the *MgO* is also very smooth. These attractive smooth surface features of the nanorods template produced in this step, thus enable the formation of smooth hollow silicon nanotubes (h-SiNTs) as well.

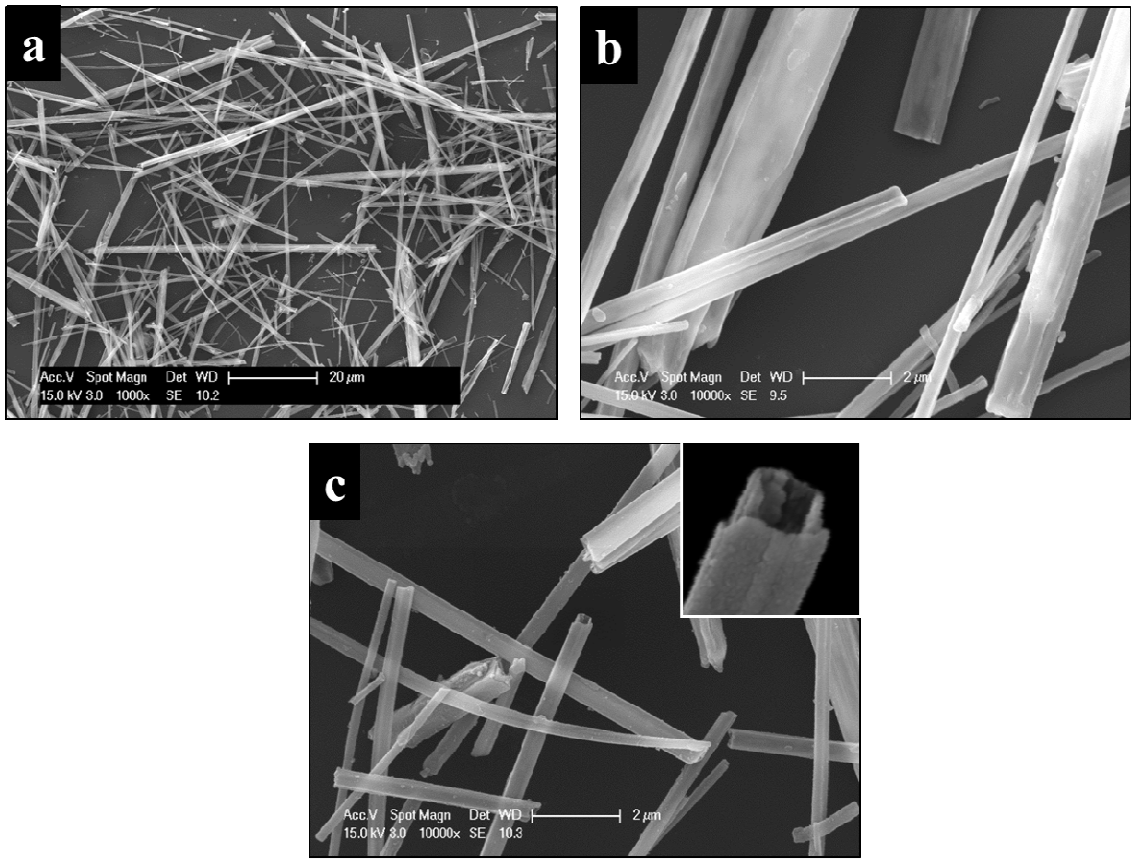

Figure 4: SEM images of (a) MgO nanorods obtained after calcination at 500^{o}C, taken at 1000X, (b) silicon coated MgO nanorods taken at 10,000X, and (c) hollow silicon nanotubes at10,000X (h-SiNTs) after etching MgO template using HCl (inset shows the open end of the nanotube taken at 80,000X showing he hollow architecture).

In the next step, the thermal cracking of silane (SiH_4) resulted in a thin uniform coating of silicon on the *MgO* nanorod templates. This results in a core-shell structure, with the inner core being *MgO* and the outer shell made of silicon. Also, as observed in **Figure 4(b)**, it should be noted that the deposition of silicon does not lead to the formation of any particles or particulate aggregates that may decrease the total yield of the nanotubes in the final product. From **Figure 4(b)**, an average increase in the thickness (50-100 nm) of the nanorods can also be observed.

The etching of the *MgO* nanorod template from the *MgO/Si* core-shell structure results in the formation of the hollow nanotubes of silicon as shown in **Figure 4(c)**. During this etching step, the chloride ions (Cl^-) from the acid bath diffuse through the silicon coating and react with *MgO* to form $MgCl_2$, which is water soluble. Following the dissolution of *MgO*, the silicon coating is well preserved resulting in the formation of hollow nanotubes of silicon. The open ends of these tubes can clearly be observed in **Figure 4(c)**. **Figure 5(a)** shows the HRTEM images of the nanotubes, wherein, the open ends of the tubes can clearly be observed**.** From these images, the silicon wall thickness can be estimated to be 60 to 80 nm. Furthermore, the high magnification image (see **Figure 5(b))** and the diffuse hollow ring observed in the selected area diffraction pattern (SAED) (**Figure 5(c))** obtained from the h-SiNT surface serve as evidence indicating that the silicon formed is amorphous and is consistent with the Raman data.

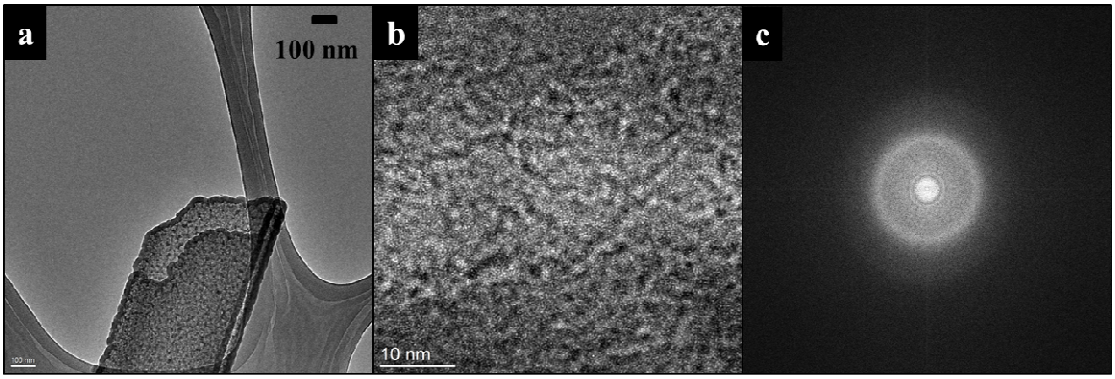

Figure 5: (a) HRTEM image of an open ended h-SiNT; (b) High magnification of h-SiNT showing the amorphous structure and (c) SAED pattern of h-SiNTs confirming the amorphous state of the nanotubes.

Template Regeneration

Most of the methods reported in the literature as mentioned earlier for generating hollow silicon nanotubes, use a sacrificial template to the best of our knowledge that cannot be regenerated. Therefore, in order to produce a new batch of silicon nanotubes, the template needs to be re-synthesized using a new set of precursors, which considerably adds to the raw material and processing costs making it quite formidable. An attractive feature of the approach outlined herein for making h-SiNTs however, is the ability to recycle or regenerate the *MgO* nanorod template which could potentially be used to repeatedly synthesize a subsequent batch of h-SiNTs. This aspect is thus extremely advantageous from a commercialization standpoint, since it does not involve continuous utilization of a new set of precursors for producing the template and the h-SiNTs.

In this approach, once the *MgO* nanorod template is dissolved using *HCl*, the filtrate mainly contains $MgCl_2$ dissolved in water and excess of *HCl*. To this solution, stoichiometric amount of sodium hydroxide (*NaOH*) equivalent to the number of moles of *HCl* is added.

This results in the precipitation of the insoluble magnesium hydroxide, $Mg(OH)_2$ from the soluble $MgCl_2$ while neutralizing the excess HCl according to the following reactions:

$$MgCl_2 + 2NaOH \rightarrow Mg(OH)_2 + 2NaCl$$

$$HCl + NaOH \rightarrow NaCl + H_2O$$

The white $Mg(OH)_2$ precipitate formed can be separated using vacuum filtration and further treated with acetic acid to form a clear solution. In this step, the hydroxide readily reacts with acetic acid to form magnesium acetate according to the reaction below.

$$Mg(OH)_2 + 2CH_3COOH \rightarrow Mg(CH_3COO)_2 + 2H_2O$$

$Mg(ac)_2$ is highly soluble in water and can easily be extracted by heating the solution to 110°C to evaporate the solvent (water). The resulting white solid when thoroughly dried is essentially composed of single phase hydrated magnesium acetate, $Mg(ac)_2.4H_2O$. The regenerated $Mg(ac)_2.4H_2O$ can thus be used along with urea in the autoclave reactor to synthesize a new set of MgO nanorods, which can further be employed to generate h-SiNTs. **Figure 6** shows the x-ray diffraction patterns of $Mg(OH)_2$ and $Mg(ac)_2.4H_2O$ obtained after the addition of $NaOH$ and acetic acid during the template recovery process, respectively. The strong low angle reflections (especially at 2θ=11°) and other smaller peaks are characteristic of the hygroscopic magnesium acetate structure and is consistent with other literature reports [21]. No other impurities or by-products such as $NaCl$ could be observed in the x-ray pattern, which indicates the efficacy of the approach and the washing processes used. Apart from the quality of the product, it is also important to have a good yield of the products obtained at different stages of the template regeneration process. **Table 1** shows the efficiency of the several reaction steps involved in the synthesis of h-SiNTs and regeneration of the starting precursor, in terms of percentage of the product obtained relative to the theoretical amount

assuming the complete conversion of the chemical reaction. It can also be observed from the **Table 1** that during the first step, only 15 % of the acetate precursors were left unreacted. However, the subsequent reactions which involves the template leaching and recovery steps are very efficient, with a conversion rate in excess of 98% demonstrating the efficiency and efficacy of the hydroxide precipitation and recovery of the soluble acetate precursor processes. Therefore, this approach is substantially simpler, cost effective and produces larger yield of the templates compared to the earlier reports [10-12] describing the generation of hollow silicon nanotube anodes for Li-ion battery applications.

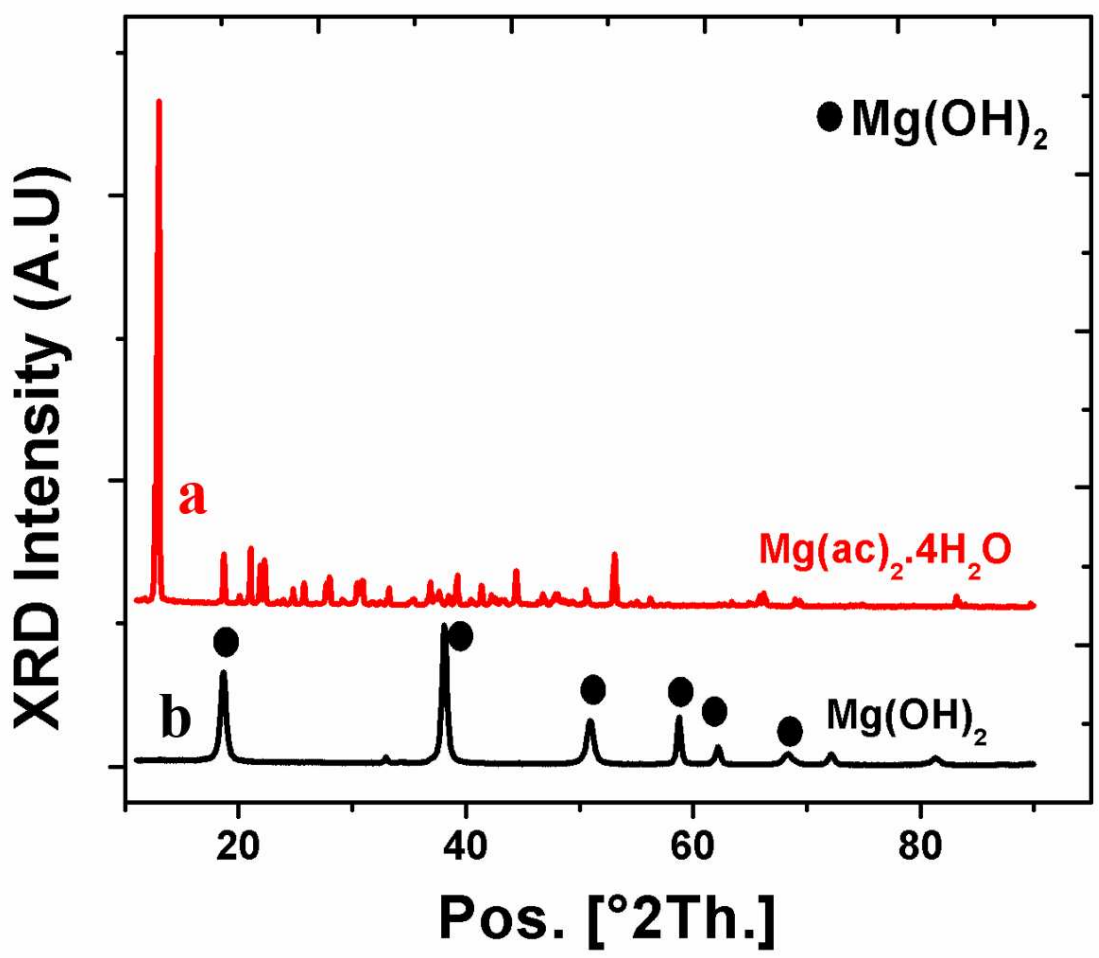

Figure 6: XRD pattern of magnesium acetate (a) and $Mg(OH)_2$ (b) obtained during the template regeneration process. NaOH reacted with the soluble $MgCl_2$ formed during the etching reaction to precipitate the insoluble $Mg(OH)_2$ (b) that is further reacted with acetic acid to form magnesium acetate (a).

Table 1: Percentage of conversion of various reactions during the MgO nanorod template synthesis and regeneration processes.

Reaction	Percentage conversion (%)
$Mg(ac)_2.4H_2O$ to $Mg(OH)_2$	84.5
$Mg(OH)_2$ to MgO	100
MgO to $MgCl_2$	98
$MgCl_2$ to $Mg(OH)_2$	99
$Mg(OH)_2$ to $Mg(ac)_2.4H_2O$	98

Electrochemical Characterization

The electrochemical properties of the h-SiNTs were investigated on electrodes generated on the copper current collectors using the conventional slurry casting method. The hollow tubular configuration of the h-SiNTs with small wall thickness (60-80 nm) contribute to the very low tap density and hence expectedly, a large amount of binder (40 wt%) is needed for achieving a good dispersion of h-SiNTs to generate a slurry that can be easily casted on the Cu current collectors. **Figure 7** shows a typical voltage vs. specific capacity plot of the h-SiNTs cycled at a medium current density of 300 $mA.g^{-1}$. The h-SiNTs exhibited a high first discharge capacity of 2615 $mAh.g^{-1}$ followed by an irreversible loss of 25%, giving rise to a charge capacity of 1970 $mAh.g^{-1}$. The small wall thickness of the nanotube configuration offers a larger exposed specific surface area of the silicon to the electrolyte, thereby contributing to a larger solid electrolyte interphase (SEI) formation, and hence consequently, the large (25%) observed first cycle irreversible (FIR) loss. Voltage plateaus can be observed in these plots during the discharge and charge processes, which are representative of the two phase regions formed by the various electrochemically active Li_xSi alloy phases. However, a better representation of these phases as a result of various alloying reactions can be identified from

the differential capacity plots shown in **Figure 8**. During the discharge or lithiation process in the first cycle, a small peak around 0.18 V followed by a large peak at 0.1 V is observed. The first peak corresponds to the voltage plateau due to the presence of two phase region between the *a-Si* and partially lithiated Li_xSi alloy.[4, 5, 18, 22] Further lithiation of this Li_xSi alloy occurs at lower voltages (~0.1 V), resulting in a completely amorphous Li_xSi alloy. During the charging or delithiation process, two peaks at 0.28 V and 0.44 V are observed which correspond to the delithiation reactions, eventually leading to the formation of *a-Si*. However, in the second cycle, the lithiation of *a-Si* occurs at relatively higher potentials (~0.24 V) and is consistent with previous reports relating to lithiation of *a-Si*.[5, 14, 18] The delithiation reactions for the second cycle occur at similar voltages, thereby indicating good reversibility and absence of any other reactions.

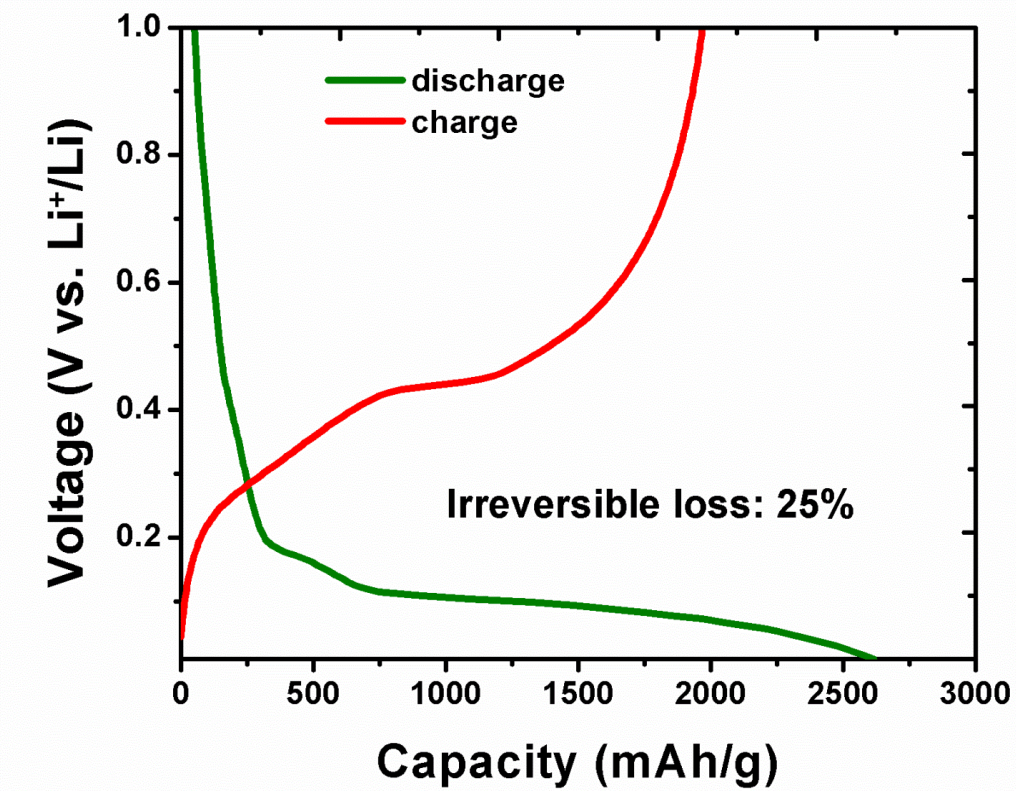

Figure 7: Voltage vs. specific capacity plot of h-SiNTs cycled at 300 $mA.g^{-1}$ in the voltage range: 0.01 to 1 V vs. Li^+/Li.

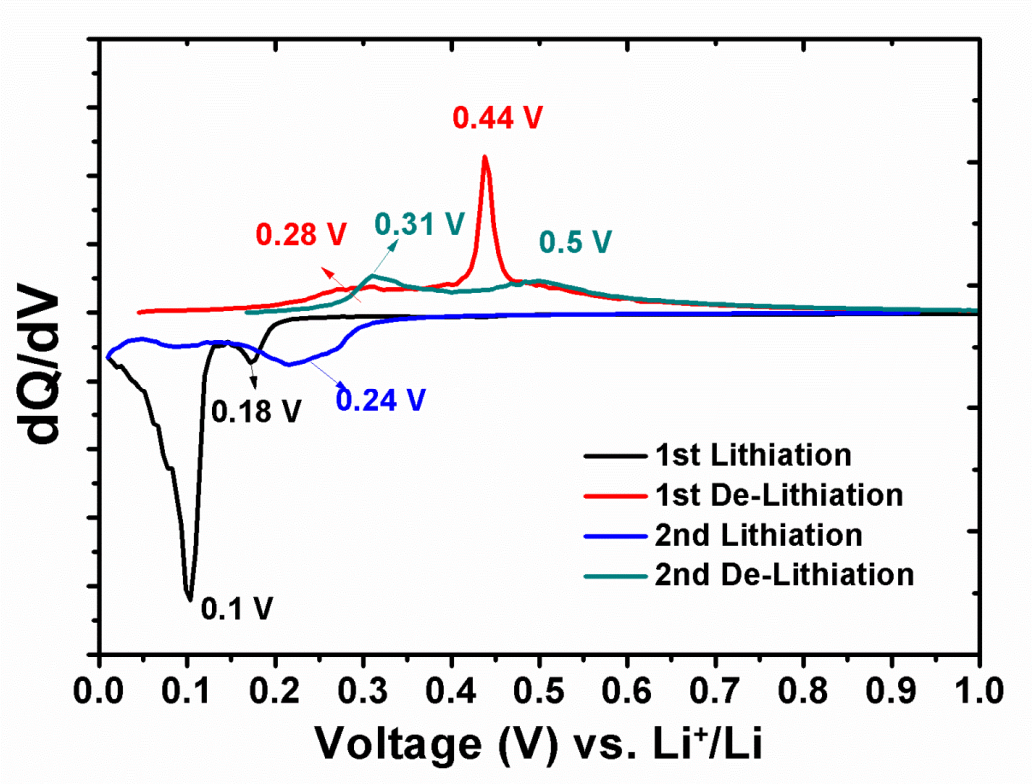

Figure 8: Differential capacity plot of h-SiNTs cycled at 300 mA.g^{-1} in the voltage range: 0.01 to 1 V vs. Li^{+}/Li.

Figure 9 shows the long term cycling of the h-SiNTs cycled at 2A.g^{-1} between the voltage range of 0.01 and 1 V vs. *Li*$^{+}$*/Li*. In this case, the first cycle test was executed by employing a current of 300 mA.g^{-1} to allow for the formation of a stable solid electrolyte interphase (SEI) on the surface of the hollow Si nanotube. As expected, when the current was switched to 2A.g^{-1}, the capacity dropped to 1551 mAh.g^{-1}. A slight increase in the specific capacity up to 1738 mAh.g^{-1} was observed for the first few cycles and this can normally be attributed to the progressive wetting of the h-SiNTs by the electrolyte especially when high current densities are used due to the kinetic limitations. The h-SiNTs nevertheless, exhibited excellent cyclability resulting in a high capacity of 1132 mAh.g^{-1} at the end of 400 cycles. This corresponds to very high capacity retention of 73% and an extremely low fade rate of

0.067% loss per cycle (for 400 cycles). The coulombic efficiency for the first 10 cycles was close to 98.5% but improved with cycling and remained close to 99.9% after 300 cycles. A corresponding voltage versus capacity plot for the long term cyclability plot is also illustrated in **Figure 10**. It is observed from this plot that after the 1st cycle, the shape of the discharge/lithiation and the charge/de-lithiation curve does not exhibit any change, indicating the good reversibility of the alloying reactions during charge and discharge stages of cycling.

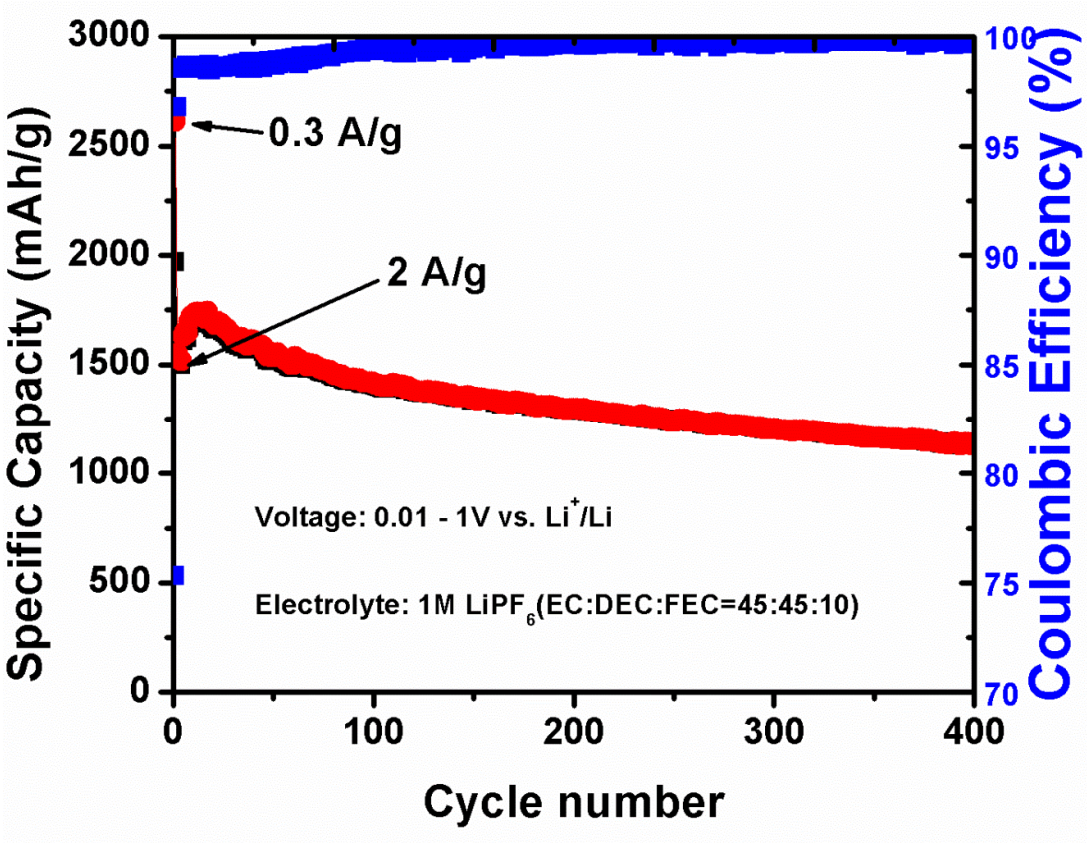

Figure 9: Long term cycling plot of h-SiNTs when cycled at 300 $mA.g^{-1}$ for the 1st cycle and $2A.g^{-1}$ for the remaining cycles in the voltage range: 0.01 to 1 V vs. Li^+/Li.

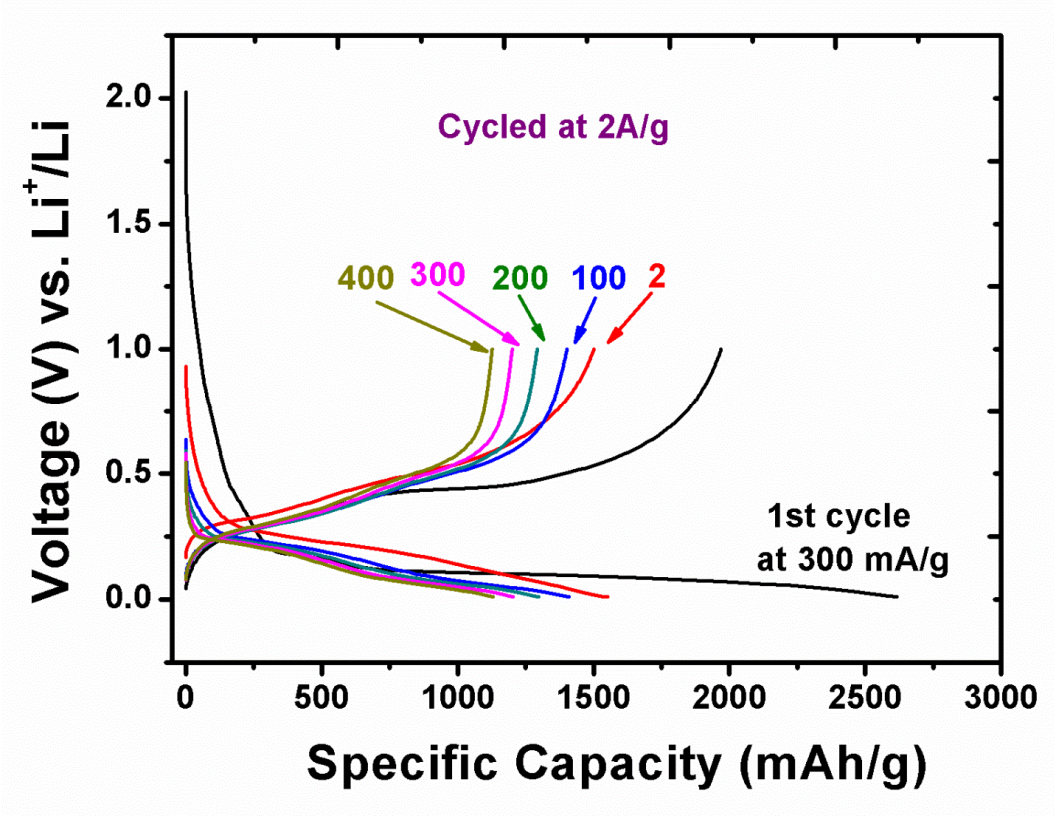

Figure 10: Voltage vs capacity plots of h-SiNTs cycled at 300 mA.g^{-1} for the 1st cycle and 2A.g^{-1} for the rest of the cycles in the voltage range: 0.01 to 1 V vs. Li^{+}/Li.

Figure 11 shows the rate capability characteristics of the h-SiNTs when cycled at different current densities (0.5 A.g^{-1}, 1 A.g^{-1}, 2 A.g^{-1} and 4 A.g^{-1}). At relatively low current densities, reversible capacities of approximately 2200 mAh.g^{-1} were obtained. However, with increasing current density to 1 A.g^{-1}, the capacity drops to only 2000 mAh.g^{-1}. Furthermore, capacities ~1700 mAh/g are obtained for a current density of 2 A.g^{-1} and finally, even at high current densities of 4 A.g^{-1}, very high specific capacities of 1300 mAh.g^{-1} are achieved. Similar or even higher capacities are regained by the system when the current densities are again lowered. This progressive increase in capacity, as discussed earlier, is likely due to the progressive wetting of the active material.

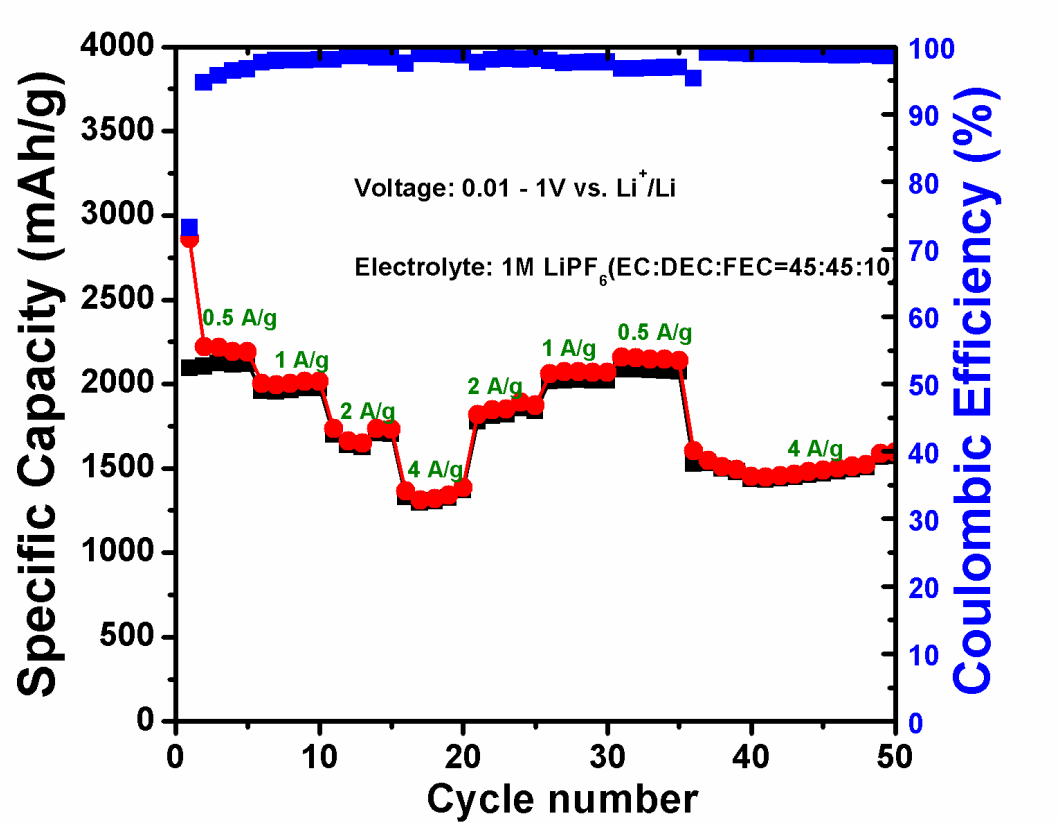

Figure 11: Rate characteristics of h-SiNTs cycled at 0.5 A.g^{-1}, 1 A.g^{-1},2 A.g^{-1},4 A.g^{-1} in the voltage range: 0.01 to 1 V vs. Li^{+}/Li

The results above demonstrate that the hollow tubular configuration of h-SiNTs allow for free expansion inwards as well as outwards of the hollow Si nanotubes during the ensuing volume expansion processes occurring when lithiated. This phenomenon can be compared to that of silicon nanowires wherein the strain upon lithiation resulted in increase of length and diameter of the nanowires without causing any pulverization. In a similar manner, the h-SiNTs are expected to undergo volume changes that result in very minimal stresses and do not result in the fracture of the nanotubes. To validate this expected stability, SEM analysis was performed on the as-cast composite electrode on copper current collector containing the h-SiNTs, binder (sodium alginate) and Super-P; analyzed again after lithiation and de-lithiation processes. The SEM images collected at different magnifications are shown in **Figure 12**.

The as-cast electrodes observed at a magnification of 10,000X clearly show the open ends of the h-SiNTs along with other electrochemically inactive species (binder and Super-P). However, after lithiation, there appears to be an increase in the average diameter of the nanotubes. This increase could be due to the volume expansion as a result of lithiation and/or due to the formation of SEI layer explained above occurring on the nanotube surface. After the de-lithiation step, a slight decrease in the diameter can be noticed, due to possible volume contraction upon de-alloying of *Li* from *Si*. Additionally, from the SEM images taken at 1000X magnification, no fracturing of the nanotubes was observed either after the lithiation or the de-lithiation processes, indicating no loss of active material at the end of the first cycle. Therefore, the origin of the large first cycle irreversible loss can be attributed only to the SEI layer formation on the nanotube surface although some contribution from the presence of trace surface oxide detected in the EDAX analysis (**Figure S1**) cannot be discounted. Furthermore, the low magnification images from all the samples appear to be similar, indicating the retention and preservation of the mechanical integrity of the composite

electrode following electrochemical cycling indicative of the remarkable stability of the hollow nanotube architectures.

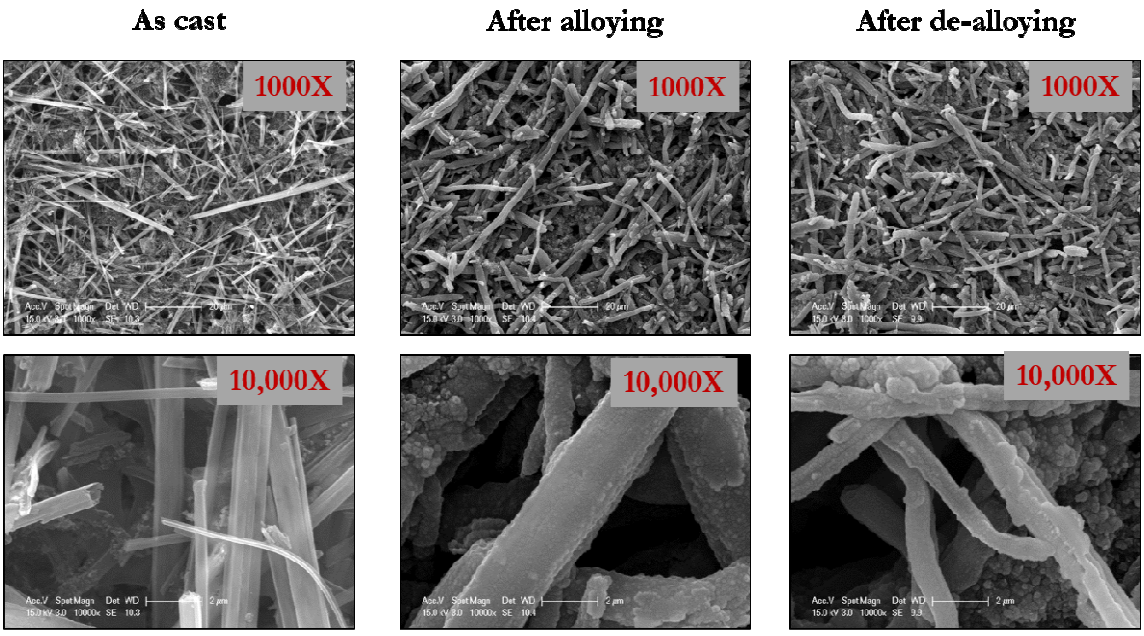

Figure 12: SEM images collected on the as-cast (top row), after lithiation (middle row), and after de-lithiation (bottom row) of the h-SiNT electrodes along with binder and Super-P imaged at different magnifications.

In this study as explained above, it is hypothesized that the excellent cyclability or capacity retention of the h-SiNTs is due to their strain engineered architecture, wherein, the repeated volume changes does not adversely affect the overall structure of the material. To validate this hypothesis, the electrode was analyzed using SEM before cycling and after it was subjected to a repeated long term cycling at a current density of 2 $A.g^{-1}$ between the voltage range 0.01 to 1 V vs. Li^{+}/Li. **Figure 13** shows the SEM images of the electrode before (left) and after 500 cycles (right) following continuous charge and discharge cycles. As described earlier, the as-cast electrode shows the uniform dispersion of h-SiNTs in the binder (sodium alginate) and Super-P. Despite using a low weight fraction of active material (50 wt%) and a

large amount of binder (40 wt%), the h-SiNTs do not appear to be enveloped inside the binder-SuperP matrix. This is due to the fact that the hollow tubular configuration of the h-SiNTs gives rise to a very low packing density material and higher volume fraction compared to its inactive counterparts (binder and Super-P). Even after 500 cycles of repeated charge and discharge processes, the one dimensional nature of the nanotubes still appears to be preserved. However, an average increase in the diameter of the nanotubes can clearly be noted, due to possible formation of SEI layer. Furthermore, a scenario could be envisioned wherein if the nanotubes were to fracture due to repeated cycling, the resulting fractured tubes would lead to loss of inter-particle contact (or loss of active material) and formation of new surfaces that could lead to additional SEI formation (or *Li* consumption). Both these phenomena would however result in a rapid capacity fade or poor cyclability, a scenario that is not witnessed and representative of the h-SiNTs developed in this study. Therefore, it can be deduced that the preservation and retention of the nanotube morphology and architecture after repeated cycling primarily contributes to and is responsible for the low capacity fade or long cycle life observed.

There is however, still some capacity loss observed at the end of 400 cycles. This decrease in capacity of the h-SiNTs after extended cycling could be due to the possible nanotubes isolation or detachment from the electrochemically inactive matrix (binder and Super-P) due to the repeated constant expansion and contraction of the nanotubes. The electrochemical performance of an anode material as is known also depends on many factors and therefore, a direct comparison of the electrochemical performance of these materials though essentially comprised of the same composition and morphology cannot be conclusively justified. The factors that affect the performance include active material loading, binder content, current rate, electrolyte composition, and more importantly, the electrode fabrication process, etc. Higher active material loading is justifiably attractive from a commercial standpoint due to the higher charge that can be stored; however, increased loading

is also known to adversely affect the cyclability of the electrode due to the obvious mass-transfer kinetic limitations. In spite of the higher loadings (0.6 to 1 $mg.cm^{-2}$) achieved in the current method, the electrochemical performance of the h-SiNTs is comparable to the earlier literature reports. For example, sealed silicon nanotubes prepared by the *ZnO* nanorods approach had a loading of 0.27 $mg.cm^{-2}$ and a capacity retention of only 82% also for only 50 cycles.[11] In another case, the double walled silicon nanotubes prepared using electrospun carbon nanofibers exhibited good cyclability, however, these nanotubes had a very low loading in the range of 0.02 to 0.1 $mg.cm^{-2}$,[10] which will likely not be attractive for commercial applications. The current approach thus bodes well and can be further optimized to generate the nanotubes with improved yields exploiting the recyclable approach towards template fabrication with correspondingly higher loading densities.

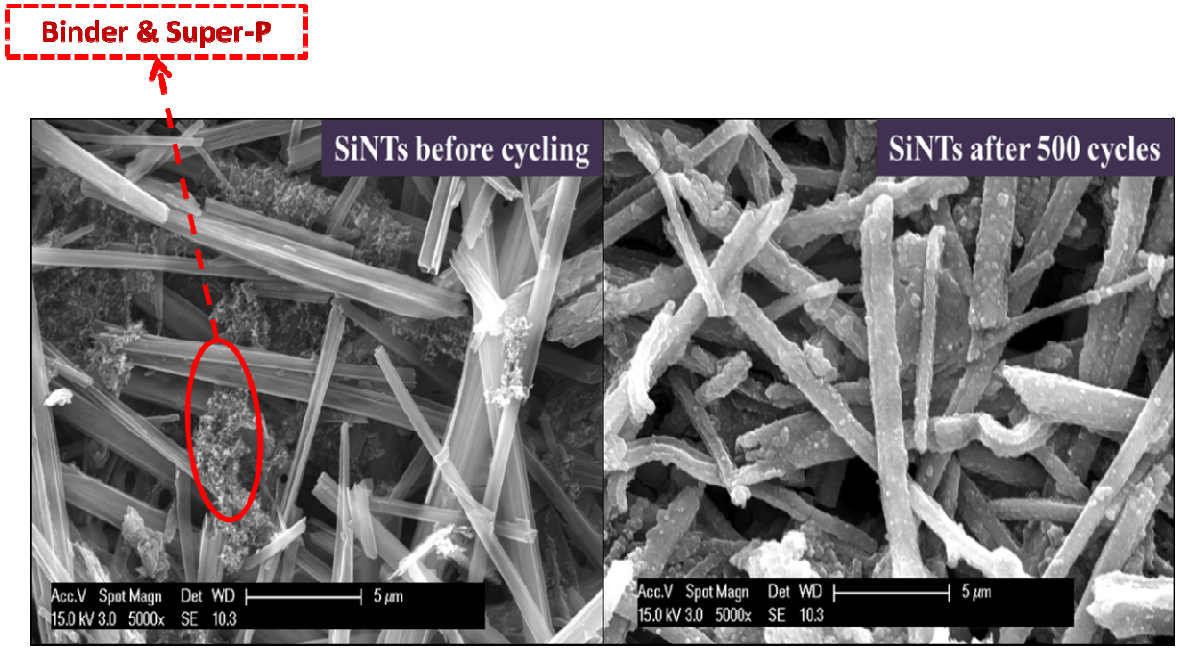

Figure 13: SEM images of h-SiNT electrodes along with binder and Super-P (a) before cycling and (b) after 500 charge-discharge cycles, cycled at a current of 2 $A.g^{-1}$ in the voltage range 0.01 to 1 V vs. Li^{+}/Li.

In order to understand the charge transfer kinetics during repeated lithiation and de-lithiation processes, impedance characteristics of the h-SiNT electrodes were analyzed at different stages of cycling providing important information on the changes occurring in the ensuing charge transfer kinetics. Accordingly, impedance spectra were collected at the end of the de-lithiation step after the 1^{st}, 100^{th}, 200^{th}, 300^{th} and 400^{th} cycles, and the resulting Nyquist plots obtained over a frequency range of 300 KHz-100 mHz are shown in **Figure 14**. In these plots, two partially overlapping semi-circular regions can be observed at higher frequencies indicative of the charge-transfer processes occurring as a result of the alloying reaction of Li^+ species with *Si.* Following this, a linear region can be observed at lower frequencies, commonly referred to as the Warburg tail. The Warburg tail is representative of mass-transfer effects related to the diffusion of Li^+ species in the bulk of the composite electrodes. The various phenomena present in the current electrochemical cell such as resistance associated with the charge transfer reaction occurring at the electrode-electrolyte interface and the SEI layer; the capacitance effect due to the adsorption of ions at various interfaces; and the diffusion phenomenon can be represented by a corresponding equivalent circuit containing elements such as resistors, capacitors, Warburg and constant phase elements (*CPEs*), etc.,

Figure 15 illustrates the equivalent circuit matching the experimentally observed response fitted using the Zview modeling software, containing a series resistor element R_s, mainly representing the solution resistance, two other RC-circuits in series representative of solid electrolyte interface (SEI) film (R_{film} and CPE_{film}) and standard processes occurring at the electrochemical double layer, Faradaic charge-transfer (R_{ct}) and double-layer capacitance (CPE_{dl}). The electron or charge transfer reactions occurring during the lithiation/de-lithiation process are modeled as the charge-transfer resistance (R_{ct}). The total charge-transfer resistance is mainly associated with the kinetics of the lithiation/de-lithiation reaction occurring at the h-SiNT surface. The active material interaction with the lithium electrolyte

and subsequent fracture due to volume changes occurring during cycling resulting in the formation of SEI film can be modeled by the use of an RC-circuit consisting of film resistance (R_{film}) and the film capacitance (CPE_{film}). In this study, we have used constant phase elements in place of capacitance elements since some asymmetry is introduced into the Nyquist plots due to the porous electrodes.[23] **Figure 14** shows that the semicircular region of the Nyquist plots obtained at different stages of cycling are superimposed and overlapping, indicating that there is no significant change in the charge-transfer resistance upon repeated cycling. **Table 2** also shows the values of the circuit elements obtained after modeling the equivalent circuit using a complex non-linear least square (CNLS) method. It can be seen that the series resistance and the film resistance values are very small indicating the facile nature of the kinetics on the h-SiNT electrodes. There is also a very gradual increase in both, the R_{film} and R_{ct} with cycling. As discussed earlier, no new active surfaces of significance are formed during repeated charge/discharge processes as observed from the post cycled SEM images of h-SiNTs (**Figure 13**) wherein the nanotubes de not exhibit any fracture even at the end of 500 cycles. The small rise in the charge transfer resistance and film resistance could possibly be attributed to the increase in the thickness of SEI layer over the course of 400 cycles of charge and discharge resulting in a gradual fade in capacity as seen in **Figure 9**. Nevertheless, the increase in R_{ct} and R_{film} values however is also very gradual reflective of the superior cycling behavior of the h-SiNTs.

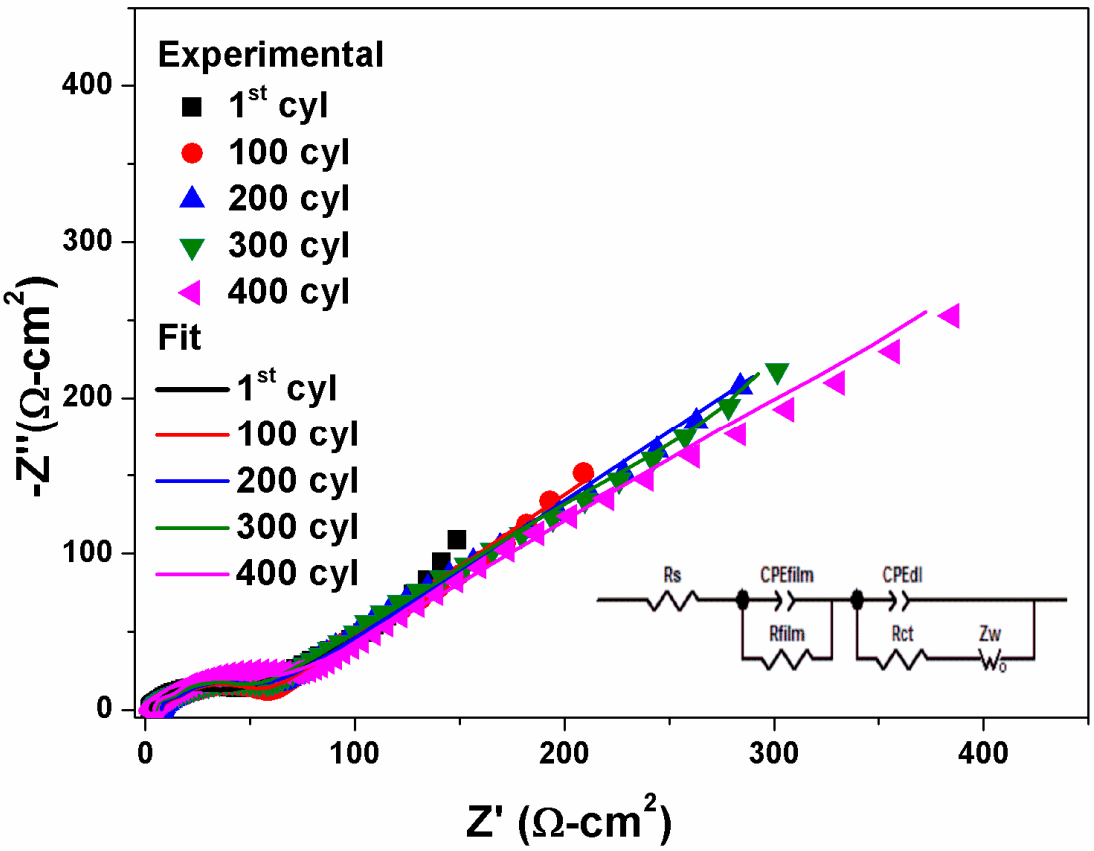

Figure 14: Impedance spectra of the h-SiNTs obtained at the end of de-lithiation step after 1st, 100th 200th, 300th and 400th cycles. Current density applied: 2A.g^{-1}, Voltage: 0.01 to 1 V vs. Li^{+}/Li.

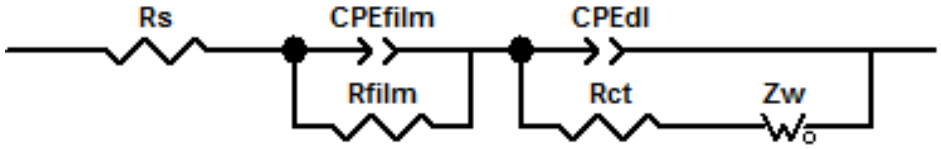

Figure 15: Equivalent circuit used for the interpretation of the impedance response of h-SiNTs (R_s: series resistance; R_{film} and CPE_{film}: film resistance and constant phase element associated with the same; R_{ct} and CPE_{dl}: charge transfer resistance associated with Li-intercalation Faradaic reactions and constant phase element associated with the electrochemical double layer; Z_w: Warburg impedance term associated with lithium mass transfer effects.

Table 2: Values of the circuit elements obtained after modeling the equivalent circuit using a complex non-linear least square (CNLS) method for EIS spectra obtained at the end of de-lithiation step after 1st, 100th, 200th, 300th and 400 cycles.

Cycle number	R_s (Ω-m^2)	CPE_{film}		R_{film} (Ω-cm^2)	CPE_{dl}		R_{ct} (Ω-cm^2)	Z_w		
		T (*10^7)	P		T (*10^6)	P		R	T	P
1	2.89	4.3	1.23	2.99	5.1	1.05	9.0	127.9	1.4	0.2
100	7.78	26.9	1.00	6.11	25.2	0.86	28.9	27.8	0.0	0.2
200	7.64	16.6	1.04	7.29	14.0	0.91	21.0	48.7	0.0	0.2
300	5.21	9.2	1.09	7.09	13.6	0.91	32.4	799.1	10.7	0.4
400	4.22	9.2	1.08	7.61	11.8	0.91	41.4	1169.0	17.8	0.4

One of the main contributions to the first cycle irreversible (FIR) loss is the irreversible consumption of lithium to form the solid electrolyte interphase (SEI) layer that is usually formed on the surface of the electrode. This layer is mainly composed of alkyl lithium carbonates *($LiOCO_2R$),* lithium carbonate *(Li_2CO_3)* and other polymers such as polycarbonate, polyethylene oxide *$(CH_2CH_2O)_n$* etc., **Figure 16** shows the FTIR spectra obtained on the h-SiNTs obtained at different stages of cycling. The peaks obtained in the absorption spectra were matched with the previously reported literature values that correspond to the various vibration and stretching modes of the SEI layer components.[24-26] It can be observed that the SEI layer formed after the first cycle contains alkyl lithium carbonates *($LiOCO_2R$),* lithium carbonate *(Li_2CO_3)* and polyethylene oxide *$(CH_2CH_2O)_n$*. However, as the cycling progressed, a significant increase in the intensity of the peaks corresponding to Li_2CO_3 are observed compared to $LiOCO_2R$ and *$(CH_2CH_2O)_n$*. This is due to further reduction of the already formed alkyl carbonates $LiOCO_2R$ during subsequent cycling to form Li_2CO_3 according to the reaction below.

$$LiOCO_2R + e^- + Li^+ \rightarrow Li_2CO_3 + R\bullet$$

The formation of Li_2CO_3 also consumes *Li* that is irreversible and may be attributed to the loss in capacity seen over several hundreds of cycles causing the increase in charge transfer resistance R_{ct} and film resistance, R_{film}. Also no additional peaks are observed in the spectra, indicating that no additional parasitic reactions are occurring during the extended cycling process.

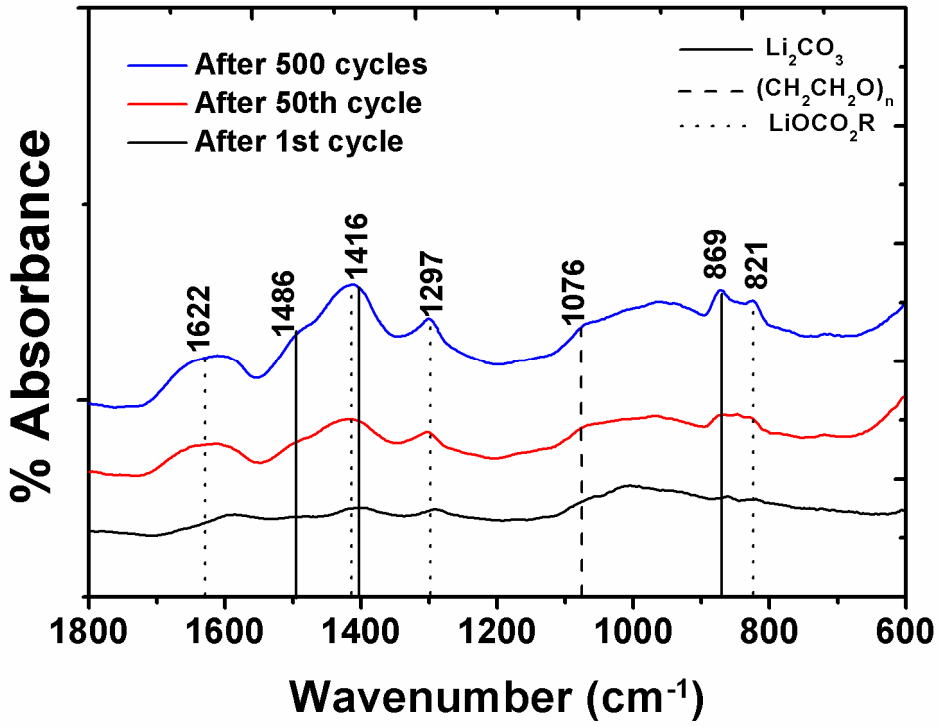

Figure 16: FTIR spectra obtained on the cycled h-SiNTs at different stages (1st , 50th and 500 cycles). The electrodes were cycled at a current density of 2A.g^{-1} between the voltage range 0.01 to 1 V vs. Li^{+}/Li. Spectra were obtained at the end of the de-lithiation step.

Additives are often added to the electrolyte to aid in augmenting certain specific functionalities such as formation of a good quality SEI layer,[27] improving the stability of $LiPF_6$ salt,[28-30] inhibiting corrosion of the *Al* current collector on the cathode side,[31] improving the wettability of the separator,[32] retarding flammability of the solvent and the electrolyte [33, 34] etc. Among them, the formation of SEI layer on the electrode surface during the first and subsequent cycles plays an important role in reducing the first cycle irreversible (FIR) loss and subsequent capacity fade, respectively. Therefore, formation of a good quality stable and non-reactive SEI layer that consumes minimal amount of Li only in the first cycle promoting reversible cycling of Li including facilitating Li-ion diffusion is absolutely essential for attaining a better battery performance and long cycle life. A good quality SEI layer is one

when initially formed, is stable and uniformly covers the electrode surface, while at the same time, preventing further electrolyte decomposition.

In this study, the h-SiNTs were tested using two commercially obtained electrolytes; one containing 3% vinylene carbonate (VC) as the additive and the other containing 10% fluoro ethylene carbonate (FEC). **Figure 17** shows the discharge capacity plots of h-SiNTs using the above mentioned additives when cycled employing identical current rates. It can be clearly observed that there is no significant difference in the first discharge capacity (2424 $mAh.g^{-1}$ using VC and 2615 $mAh.g^{-1}$ using FEC) and first cycle irreversible loss (24% using VC and 25% using FEC). However, the h-SiNTs cycled using the electrolyte containing FEC additive exhibited better cyclability compared to the electrode cycled using electrolyte containing VC. In the case of VC, the specific capacity decreased rapidly during the first 100 cycles, resulting in a capacity of only 748 $mAh.g^{-1}$ at the end of 400 cycles, corresponding to a capacity retention of only 51 % (fade rate: 0.122% loss per cycle). On the other hand, h-SiNTs cycled using the electrolyte containing FEC additive exhibited a capacity of 1132 $mAh.g^{-1}$ at the end of 400 cycles resulting in a higher capacity retention of 73% (fade rate: 0.067% loss per cycle). Though VC and FEC are reported to improve the cyclability of negative electrodes for lithium-ion batteries, electrolytes containing more than 2% VC (by weight) have been shown to have greater charge transfer resistance compared to electrolytes containing FEC.[35] A poor and non-uniform coating of SEI layer could thus result in the larger charge transfer resistance in the case of VC based electrolytes. This results in relatively sluggish kinetics when operated at high current densities such as $2A.g^{-1}$, thus leading to lower specific capacities or inferior cyclability as is the case observed in **Figure 17** for the h-SiNT electrodes cycled using electrolytes containing VC.

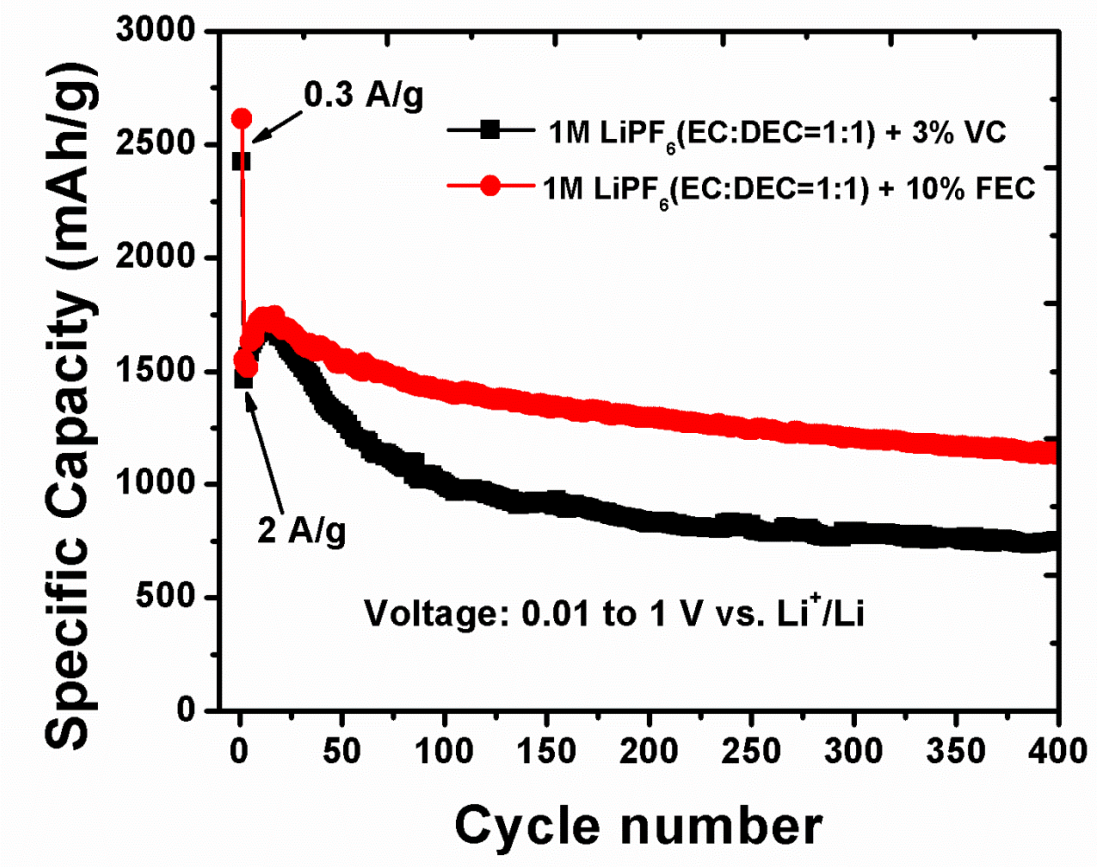

Figure 17: Discharge capacities of h-SiNTs using VC and FEC as additives to the LiPF6 electrolyte cycled at 300 $mA.g^{-1}$ for 1st cycle and $2A.g^{-1}$ for the rest of the cycles between the voltage range: 0.01 to 1 V vs. Li+/Li

3. Experimental Section

Synthesis of MgO nanorods

Magnesium oxide nanorods were synthesized according to a modified published method.[36] Specifically 6.44 g of magnesium acetate tetrahydrate (Aldrich) and 1.2 g of urea was dissolved in 75 ml and 25 ml of DI water, respectively. The urea solution was added drop wise to the acetate solution under vigorous stirring and left for an hour. The solution was then

added to a Teflon lined stainless steel autoclave (125 ml total capacity) and heated to 180°C at 5C/min for 1h. At the end of the reaction, the vessel was allowed to cool down to room temperature before it was opened. A white precipitate was observed which was washed thrice thoroughly with DI water and isopropanol to remove any unwanted dissolved products and collected on 0.5 μm PTFE membrane using vacuum filtration. The wet cake at the end of filtration was then dried in a 60°C oven overnight to evaporate the solvent. This wet cake is mainly composed of nanorods of magnesium hydroxide $(Mg(OH)_2$. A final calcination step on these $Mg(OH)_2$ nanorods was performed in pure oxygen gas by first heating from room temperature to 310°C at a heating rate of 3°C/min for 7 hours and then to 500°C at 1°C/min for 1hour, resulting in a *MgO* nanorod cake.

Synthesis of h-SiNTs

The dried *MgO* nanorod cake after vacuum drying was coated with a uniform amorphous *Si* coating using a low pressure chemical vapor deposition system (LPCVD). 2% silane (SiH_4) diluted in argon gas was decomposed at 500°C for 10 minutes. The core-shell *Si/MgO* cake was then dispersed in 6N *HCl* solution and homogenized in a bath sonicator for 2 hours to dissolve the underlying *MgO* nanorods. After dissolution, the hollow silicon tubes (h-SiNTs) were thoroughly washed with DI water and isopropanol and were collected on 0.5 μm PTFE membrane filters using vacuum filtration. Finally, the solvent from the wet h-SiNT cake was removed by heating to 100°C overnight in a drying oven.

MgO template regeneration

The supernatant left after washing the *Si/MgO* core-shell structure comprises mainly of $MgCl_2$ dissolved in water and excess *HCl*. *NaOH* was added to the precipitate, $Mg(OH)_2$ and the excess *HCl* will react with *NaOH* to form *NaCl* which further dissolves in water. The white suspension was centrifuged and filtered over 0.5 μm PTFE membrane to obtain a white solid.

To this white solid *($Mg(OH)_2$)*, stoichiometric amount of acetic acid was added, stirred for 2 hours and the concentration adjusted to 86 $mg.ml^{-1}$. 75 ml of this regenerated magnesium acetate solution was then used to prepare the second generation of *MgO* nanorod template.

Characterization

For phase analysis, x-ray diffraction studies were performed using Philips X'Pert Pro system with *Cu Kα*, λ = 0.15406 nm radiation. Raman spectroscopy was performed using a 633 nm red diode laser using a Renishaw in via microscope. Morphological studies were performed using a Philips XL30 (10-20 KV operating voltage) scanning electron microscope (SEM) equipped with an energy dispersive x-ray spectroscopy (EDAX) analyzer. High resolution transmission electron microscopy (HRTEM) studies were conducted using the JEOL JEM-2100F microscope.

Electrochemical testing

Slurries of the h-SiNTs were prepared by mixing 50 wt% of active material (h-SiNTs) with 40 wt% binder (sodium alginate, MP Biomedicals) and 10 wt% Super-P (MTI Corp) in DI water for atleast 8 hours to ensure good dispersion. The slurries were then degassed for few minutes before being cast onto copper foils which were later dried in air for 1 hour and then in vacuum at 100°C overnight. An electrode loading in the range 0.6 – 1 mg/cm^2 was achieved on the cut copper foils. CR 2025 coin cells (MTI Corp) were used where *Li* metal and Celgard 2250 served as the cathode and separator, respectively. The electrolyte used in all the studies was 1M *$LiPF_6$* in ethylene carbonate/diethyl carbonate/fluoroethylene carbonate (45:45:10, BASF) except in the case when 3% vinylene carbonate was used with EC and DEC constituting 97%. Electrochemical testing was done within the voltage range 0.01 - 1 V vs. *Li^+/Li* in a galvanostatic current mode. Impedance studies of the electrodes were performed using a

Gamry potentiostat in a frequency range 0.1 Hz to 300,000 Hz with 10 mV amplitude and no applied potential bias.

4. Conclusions

The results discussed above demonstrate a facile and inexpensive approach that was developed for producing scalable quantities of hollow silicon nanotubes (h-SiNTs) (nearly 0.5 g of final product using only 15 minutes of silicon deposition). A sacrificial *MgO* nanorod template was first synthesized in an autoclave reactor by hydrothermal synthesis approach, onto which amorphous silicon was the deposited as a thin layer by CVD to form a core-shell structure. The *MgO* core was subsequently dissolved by acid etching to generate hollow nanotubes of silicon (h-SiNTs). These h-SiNTs exhibited high specific capacities, excellent cycling stability and good rate capability. A first discharge capacity of 2615 $mAh.g^{-1}$ and a charge capacity of 1970 $mAh.g^{-1}$ were obtained employing 300 $mA.g^{-1}$ current density, corresponding to 25% first cycle irreversible loss. The h-SiNTs exhibited a high capacity retention of 73% at the end of 400 cycles corresponding to a very low fade rate of only 0.067% loss per cycle. The excellent cyclability demonstrated by the sacrificial template derived h-SiNTs was further validated by SEM images of post post-cycled electrodes whereby it was observed that the hollow tube structure was still preserved, despite the volume expansion of silicon during 400 cycles of charge and discharge. Additionally, a closed loop regenerative process using simple dissolution and precipitation techniques was developed to regenerate the starting precursor, $Mg(ac)_2.4H_2O$ with high purity demonstrating the cost effectiveness, efficacy, and recyclable nature of this h-SiNT generation process.

Acknowledgements

The authors gratefully acknowledge the financial support provided by the Assistant Secretary for Energy Efficiency and Renewable Energy, Office of Vehicle Technologies of the U.S. Department of Energy under Contract No. DE-AC02-05CH11231, subcontract No. 6951369, under the Batteries for Advanced Transportation Technologies (BATT) program. The authors also acknowledge the National Science Foundation (NSF-CBET-0933141) and partial support of the Ford Foundation. Financial assistance from the Edward R. Weidlein Chair Professorship funds and the Center for Complex Engineered Materials (CCEMM) for partial support of this research is also acknowledged by PNK.

References

1. J. M. Tarascon and M. Armand, *Nature*, 2001, 414, 359-367.
2. C. K. Chan, H. L. Peng, G. Liu, K. McIlwrath, X. F. Zhang, R. A. Huggins and Y. Cui, *Nat. Nanotechnol.*, 2008, 3, 31-35.
3. L. F. Cui, R. Ruffo, C. K. Chan, H. L. Peng and Y. Cui, *Nano Lett.*, 2009, 9, 491-495.
4. R. Epur, M. K. Datta and P. N. Kumta, *Electrochimica Acta*, 2012, 85, 680-684.
5. W. Wang, R. Epur and P. N. Kumta, *Electrochem. Commun.*, 2011, 13, 429-432.
6. W. Wang and P. N. Kumta, *Acs Nano*, 2010, 4, 2233-2241.
7. K. Evanoff, J. Benson, M. Schauer, I. Kovalenko, D. Lashmore, W. J. Ready and G. Yushin, *Acs Nano*, 2012, 6, 9837-9845.
8. L. David, D. Asok and G. Singh, *ACS applied materials & interfaces*, 2014, 6, 16056-16064.
9. Y. Yao, M. T. McDowell, I. Ryu, H. Wu, N. Liu, L. Hu, W. D. Nix and Y. Cui, *Nano Lett.*, 2011, 11, 2949-2954.
10. H. Wu, G. Chan, J. W. Choi, I. Ryu, Y. Yao, M. T. McDowell, S. W. Lee, A. Jackson, Y. Yang, L. B. Hu and Y. Cui, *Nat. Nanotechnol.*, 2012, 7, 309-314.
11. T. Song, J. L. Xia, J. H. Lee, D. H. Lee, M. S. Kwon, J. M. Choi, J. Wu, S. K. Doo, H. Chang, W. Il Park, D. S. Zang, H. Kim, Y. G. Huang, K. C. Hwang, J. A. Rogers and U. Paik, *Nano Lett.*, 2010, 10, 1710-1716.
12. M. H. Park, M. G. Kim, J. Joo, K. Kim, J. Kim, S. Ahn, Y. Cui and J. Cho, *Nano Lett.*, 2009, 9, 3844-3847.
13. Z. Lu, T. Wong, T.-W. Ng and C. Wang, *RSC Advances*, 2014, 4, 2440-2446.
14. R. Epur, M. K. Datta and P. N. Kumta, *Electrochimica Acta*, 2012, 85, 680-684.
15. R. L. C. Vink, G. T. Barkema and W. F. van der Weg, *Physical Review B*, 2001, 63, 115210.

16. J. H. Parker, Jr., D. W. Feldman and M. Ashkin, *Physical Review*, 1967, 155, 712.
17. C. Smit, R. van Swaaij, H. Donker, A. Petit, W. M. M. Kessels and M. C. M. van de Sanden, *Journal of Applied Physics*, 2003, 94, 3582-3588.
18. M. K. Datta, J. Maranchi, S. J. Chung, R. Epur, K. Kadakia, P. Jampani and P. N. Kumta, *Electrochimica Acta*, 2011, 56, 4717-4723.
19. R. Epur, L. Minardi, M. K. Datta, S. J. Chung and P. N. Kumta, *Journal of Solid State Chemistry*, 2013, 208, 93-98.
20. R. Epur, M. Ramanathan, F. R. Beck, A. Manivannan and P. N. Kumta, *Materials Science and Engineering B-Advanced Functional Solid-State Materials*, 2012, 177, 1151-1156.
21. S.-W. Bian, J. Baltrusaitis, P. Galhotra and V. H. Grassian, *Journal of Materials Chemistry*, 2010, 20, 8705-8710.
22. L.-F. Cui, R. Ruffo, C. K. Chan, H. Peng and Y. Cui, *Nano Lett.*, 2008, 9, 491-495.
23. J. R. Macdonald and E. Barsoukov, *History*, 2005, 1, 8.
24. S. Tsubouchi, Y. Domi, T. Doi, M. Ochida, H. Nakagawa, T. Yamanaka, T. Abe and Z. Ogumi, *Journal of The Electrochemical Society*, 2012, 159, A1786-A1790.
25. D. Aurbach, M. D. Levi, E. Levi and A. Schechter, *The Journal of Physical Chemistry B*, 1997, 101, 2195-2206.
26. D. Aurbach, Y. Ein‐Ely and A. Zaban, *Journal of The Electrochemical Society*, 1994, 141, L1-L3.
27. C. Korepp, H. J. Santner, T. Fujii, M. Ue, J. O. Besenhard, K. C. Möller and M. Winter, *Journal of Power Sources*, 2006, 158, 578-582.
28. S. S. Zhang, K. Xu and T. R. Jow, *Electrochemical and solid-state letters*, 2002, 5, A206-A208.
29. J. Wang, *Electroanalysis*, 2005, 17, 7-14.
30. W. Li, C. Campion, B. L. Lucht, B. Ravdel, J. DiCarlo and K. M. Abraham, *Journal of The Electrochemical Society*, 2005, 152, A1361-A1365.
31. L. J. Krause, W. Lamanna, J. Summerfield, M. Engle, G. Korba, R. Loch and R. Atanasoski, *Journal of Power Sources*, 1997, 68, 320-325.
32. X. Wang, H. Naito, Y. Sone, G. Segami and S. Kuwajima, *Journal of The Electrochemical Society*, 2005, 152, A1996-A2001.
33. X. Wang, E. Yasukuwa and S. Kasuya, *Journal of The Electrochemical Society*, 2001, 148, A1058-41065.
34. K. Xu, S. Zhang, J. L. Allen and T. R. Jow, *Journal of The Electrochemical Society*, 2002, 149, A1079-A1082.
35. D. Y. Wang, N. N. Sinha, J. C. Burns, C. P. Aiken, R. Petibon and J. R. Dahn, *Journal of The Electrochemical Society*, 2014, 161, A467-A472.
36. F. Al-Hazmi, F. Alnowaiser, A. A. Al-Ghamdi, M. M. Aly, R. M. Al-Tuwirqi and F. El-Tantawy, *Superlattices and Microstructures*, 2012, 52, 200-209.